energy&fuels

pubs.acs.org/EF Article

Pore Structure Alteration of Organic-Rich Shale with Sc-CO_2 Exposure: the Bakken Formation

Ogochukwu Ozotta, Kouqi Liu, Thomas Gentzis, Humberto Carvajal-Ortiz, Bo Liu, Saeed Rafieepour, and Mehdi Ostadhassan*

Cite This: https://dx.doi.org/10.1021/acs.energyfuels.0c03763 Read Online

ACCESS | Metrics & More | Article Recommendations

ABSTRACT: The interaction between various components of shale and CO_2 is interesting since it alters pore structures that are the governing factor in different projects. In this study, samples from the Upper (UB) and Lower (LB) Bakken were exposed to super critical CO_2 for 3, 8, 16, 30, and 60 days. Then, chemical and structural changes during the process of exposure were evaluated with different methods, including X-ray diffraction (XRD), gas adsorption (N_2) isotherm, and fractal theory. The results showed that quartz increased in the UB and decreased in the LB, whereas clay and other minerals had a decreasing trend for both UB and LB after CO_2 saturation. After saturation, the pore size distributions (PSDs) were skewed to smaller pore sizes at all diameters, indicating that the number of pores decreased as a result of the reaction. Fractal dimension has an increasing trend as the samples were exposed to CO_2, where the roughness of the pore surface and the complexity of pore structure increased after 8−16 days of CO_2 saturation and then decreased after 30−60 days of saturation to become more homogeneous. Furthermore, clay mineral dissolution enhanced the pore volume, and carbonate dissolution increased the specific surface area. These results provided experimental evidence to further test the mechanisms of geological storage of CO_2 in organic-rich self-sourced plays.

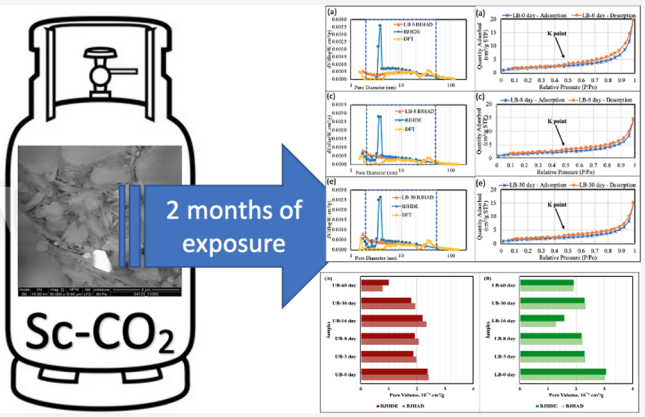

1. INTRODUCTION

The importance of unconventional shale plays in today's energy supply has driven a considerable amount of research in the past decade to various directions in petroleum engineering and geosciences. This is because of the complex nature of shale rocks that is heterogeneous and anisotropic.[1,2] This complexity originates from the pore structure and the presence of various constituent components (mineral matrix and organic matter) in such lithology. Different sizes of pores exist in shale rock and are not distributed uniformly while ranging from nano to micrometer in size.[3] Such pores can be isolated or connected and can be found within the matrix or the organic matter. To be more specific, pores with a diameter greater than 50 nm are classified as *macropores*, and those between 2 and 50 nm are classified as *mesopores*. Pores with a diameter not exceeding 2 nm are *micropores* according to the International Union of Pure and Applied Chemistry (IUPAC),[4] and all can be found in shale samples.[3] In this regard, total porosity, pore distribution, and specific surface area (SSA) are some of the quantitative characteristics of pore structures that should be known for geophysical, petrophysical, and geomechanical modeling of any porous material.[5−7] Furthermore, storage and fluid conductivity of organic rich shales are highly dependent on pore structures[5−7] and become even more significant in enhanced oil recovery (EOR) with CO_2 and/or carbon capture and sequestration (CCS) operations.[6−8] Organic-rich shale, as defined by Duncan and Swanson,[9] is a fine-textured sedimentary rock containing about 5 to 65% by weight of naturally occurring organic matter (kerogen). Organic-rich shales consist of reduced carbon primarily and smaller amounts of hydrogen, oxygen, nitrogen, and sulfur. The increase of the total organic carbon (TOC) in shales can decrease the porosity because of the occurrence of nonporous organic matter[10] and becomes altered with increased thermal maturation.

Considering the significance of pore structure evaluations, a wide range of methods have been used to analyze and characterize pore structures of shales, including gas adsorption

Received: November 8, 2020
Revised: January 24, 2021

methods,[3,11,12] mercury intrusion porosimetry (MIP),[13,14] small angle neutron scattering (SANS), ultrasmall angle neutron scattering (USANS),[15] and nuclear magnetic resonance (NMR).[16] There are other direct observation methods such as field emission scanning electron microscopy (FE-SEM),[10,17,18] atomic force microscopy (AFM),[19,20] microfocus X-ray computed tomography (u-CT),[21,22] and transmission electron microscopy (TEM).[23] Each of these methods has its advantages and disadvantages and can provide specific information about the pore size distribution (PSD), porosity, geometric, morphological details, and other quantitative measures of shale rock pore structures.[3] For example, MIP, instead of measuring the true pore size, determines the largest entrance of mercury into the pore.[24] FE-SEM cannot provide information about the micropores because of the limitations in tool resolution but can directly detect size and distribution of larger pores.[12] A collection of gas adsorption techniques would be necessary to obtain an entire spectrum of pore size distribution (PSD), from the submicron to the macroscale. In addition to understanding the porosity and PSD of the shale rock quantitatively, another major parameter affecting flow properties and storage capacity is the complexity of the pore network.[3] This becomes more important when the formation is a target for CO_2 EOR or CCS since pore structure parameters become altered during exposure to carbon dioxide.

CO_2 EOR and CCS are two types of operations that are becoming prominent in organic-rich shale formations, such as the Bakken. In both of these processes, the rock gets exposed to CO_2, and when the gas is injected into the shale layers, it dissolves and changes the acid−base equilibrium that triggers the dissolution and precipitation of minerals.[25,26] As a result of dissolution, flow channels can be formed in the rock, which will eventually alter the intrinsic permeability and porosity of the rock. This can also induce changes in the microstructures of the material if the exposure time is long enough, presenting itself as changes in pore size and pore connectivity. Ultimately, this will cause retention capabilities of the rock matrix and the organic matter as well as its capability to conduct fluids to deteriorate or improve.[27] The phase state of CO_2 has a significant influence on the CO_2−shale interaction as found in the study of Pan et al.[14] Supercritical CO_2 ($ScCO_2$) has a greater influence on the shale pore structure than subcritical CO_2 ($SubCO_2$), and the change in the pore structure parameter is also related to the shale sample.[28] One study found that pores with diameters less than 100 nm were developed in a marine shale sample after exposure to CO_2, which was interpreted to be due to the complex chemical reactions caused by CO_2 saturation.[14] Okamoto et al.[29] suggested that supercritical CO_2 ($ScCO_2$) has a stronger solubility and can modify organic matter and dissolve more minerals when injected at higher pressures to improve the porosity and permeability of the medium.[29] Considering that the common elements in shales are C, O, Mg, Al, Si, S, K, and Ca,[9,30,31] Caroll et al.[32] reported that CO_2 has an effect on the properties of shale, especially dissolution of siliceous and carbonate minerals. Calcite dissolution is more common in carbonate-rich formations, which softens the pore contacts and then changes the pore geometry and, eventually, the microstructure of the material. Some studies have shown that dry CO_2 can dissolve the minerals in shale, such as montmorillonite, kaolinite, and calcite, which further contributes to changes in shale pore structures.[33,34] Yin et al.[33] reported that the pore structure and mineral composition in shale were altered after exposure to $ScCO_2$, finding that the content of clay and carbonates minerals in the shale decreased, the specific surface area of the shale decreased, and the average pore size increased due to the extraction or dissolution effect of CO_2 and CO_2-adsorption induced swelling. Exposure of mudrocks to supercritical CO_2 at different temperatures and pressures also controls the dissolution quantity and can increase it.[35] Jiang et al. reported an increase in the specific surface area and porosity and that $ScCO_2$ would be capable of extracting organic matter in shale and dissolving primary pores and fractures of the Longmaxi Formation.[36] Collectively, interaction of $ScCO_2$ and shale causes microscopic pore structure changes with the influence of temperature and pressure.[29,35,36] Since a high adsorption preference of shale for CO_2 is well proven,[37−39] Sorensen et al.[6] calculated the CO_2 storage capacity of the Bakken Formation ranging from 121 megatons (Mt) to 3.2 gigatons (Gt), concluding that a more accurate estimation would require additional detailed information about the pore structures and subsequent changes after the formation is exposed to CO_2.

Considering the above, a proven tool to interpret pore structure data from any complex porous media is through fractal theory. This theory, first suggested by Mandelbrot,[40] has also been commonly used for the study and quantification of the complexity and heterogeneity of pore structures.[12,34,41,42] The fractal dimension should be in the range of 2−3 according to fractal theory.[43,44] Given the increasing complexity and heterogeneity of shale pores, fractal dimension generally increases. Fractal measurements can be estimated using the appropriate model, based on experiments with gas adsorption, such as the Lagmuir model, Frenkel−Halsey−Hill (FHH) model, fractal BET model, and thermodynamic method.[45−47] Research into fractal characteristics based on the FHH model and N_2 adsorption experiment data is widely used to quantitatively describe the pore structure in shale.[33,41,42]

The Bakken and similar organic-rich shale plays are becoming the target for CCS and EOR simultaneously. Hence, this article attempts to study the changes that will occur to the pore structures when the shale is exposed to carbon dioxide for a long period of time. In this study, alterations to the pore structure of the Bakken Shale at various times of exposure to $ScCO_2$ are evaluated. Changes investigated include mineral dissolution and quantification of several pore structure parameters such as the PSD, porosity, and surface area. This information would ultimately enable us to develop an appropriate injection strategy, estimate injection potential, and quantify injection induced seismicity risks for a more successful sequestration and EOR process in the Bakken and similar formations.

1.1. Geology of the Research Area. The Bakken Formation is a major unconventional petroleum play in the Williston Basin which spreads through North Dakota and Montana in the United States and Saskatchewan in Canada and is the second largest shale play in the United States of America. The Bakken is of Late Devonian−Early Mississippian age and consists of the upper, middle, and lower members.[48] The Bakken play holds about 3.6 billion barrels of recoverable oil, 1.85 trillion cubic feet of dissolved gas, and 148 million barrels of natural gas liquids.[49] The Upper and Lower Bakken are dark marine shales with high organic content and are referred to as the source and seal rock in the Bakken, while the middle member is a middle fine-grained combination of clastic and carbonates, calcareous or dolomitic siltstone, and sand-

https://dx.doi.org/10.1021/acs.energyfuels.0c03763
Energy Fuels XXXX, XXX, XXX−XXX

Table 1. Mineralogical Composition of the Samples (in wt %) before CO_2 Saturation for the Upper Bakken and for the Lower Bakken Samples

CO_2 exposure days	name	quartz	pyrite	calcite	dolomite	clay minerals[a]	others	TOC%	T_{max}°C
0 day	UB-0	18.7	3.0	3.9	0.0	50.5	23.9	13.3	449.0
0 day	LB-0	53.0	3.0	3.0	9.0	19.0	13.0	14.4	448.0

[a]Clay minerals: illite + kaolinite + chlorite.

stone known as the tight reservoir.[50,51] The middle member, which is the reservoir, has a porosity between 1% and 15% and a permeability of <0.1 millidarcies.[2,6,52] Furthermore, while all three types of pores exist in the Bakken Formation, the upper and lower members have dominant micropores, but mesopores and macropores are the main contributors to the overall porosity of the Bakken.[12] Ultimately, the Bakken Formation has natural fractures too which act at the secondary porosity in the Middle Bakken.[53]

2. METHODOLOGY

2.1. Sample Preparation. Samples from the upper and lower members of the Bakken Formation (source rocks) were retrieved from cores that are stored in the North Dakota Geological Survey Core Library located at the University of North Dakota. Samples were dried, crushed, and sieved with <250 μm mesh for homogenization. A portion of the crushed sample was used for laboratory analysis before CO_2 saturation, and the rest was put in a Vinci hydrostatic core holder for saturation and varying exposure times. The core holder was connected to a high-pressure CO_2 cylinder, while the pressure was monitored with a regulator on the cylinder to ensure $ScCO_2$ conditions were maintained. The core holder was tightly closed, leaving the valve open to bleed the CO_2 from the connection pipes before shutoff. The CO_2 saturation was set at a pressure of about 1020 psi (supercritical) and room temperature. After 3 days of CO_2 saturation, the core holder was opened to collect crushed samples for laboratory analysis. This procedure was repeated for 8 days, 16 days, 30 days, and 60 days of saturation/exposure to CO_2 under similar pressure and temperature conditions. A total of 12 samples were prepared for geochemistry, mineralogical and pore structure analyses at each stage and prior to the incubation process (Tables 1−4).

Table 2. Mineralogical Composition of the Samples (in wt %) after CO_2 Saturation for the Upper Bakken Sample

CO_2 exposure days	0 day	3 days	8 days	16 days	30 days	60 days
name	UB-0	UB-3	UB-8	UB-16	UB-30	UB-60
quartz	18.7	24.8	16.4	35.0	34.8	35.0
pyrite	3.0	4.0	16.0	2.8	5.3	2.5
calcite	3.9	6.0	2.2	4.9	3.3	6.8
dolomite	0.0	1.0	3.2	4.2	0.0	0.5
clay mineral[a]	50.5	26.1	43.0	18.2	7.4	12.6
others	23.9	38.1	19.2	34.9	49.2	42.6
CO_2 exposure days	0 day	3 days	8 days	16 days	30 days	60 days
clay minerals	UB-0	UB-3	UB-8	UB-16	UB-30	UB-60
illite	35.5	24.1	35	10.6	2.4	9.1
kaolinite	15	0	0	6.6	4.4	2.5
chlorite	0	2	8	1	0.6	1

[a]Clay minerals breakdown for the UB samples.

Table 3. Mineralogical Composition of the Samples (in wt %) after CO_2 Saturation for the Lower Bakken Sample

CO_2 exposure days	0 day	3 days	8 days	16 days	30 days	60 days
name	LB-0	LB-3	LB-8	LB-16	LB-30	LB-60
quartz	53.0	45.0	44.0	33.0	45.0	42.0
pyrite	3.0	3.0	1.0	3.0	2.0	4.0
calcite	3.0	1.0	0.0	6.0	2.0	10.0
dolomite	9.0	3.0	3.3	9.0	4.0	5.0
clay mineral[a]	19.0	25.0	23.0	22.0	20.0	17.6
others	13.0	23.0	28.7	27.0	27.0	21.4
CO_2 exposure days	0 day	3 days	8 days	16 days	30 days	60 days
clay minerals	LB-0	LB-3	LB-8	LB-16	LB-30	LB-60
illite	10	19	19	14	15	15
kaolinite	9	3	4	1	0	2.6
chlorite	0	3	0	7	5	0

[a]Clay minerals breakdown for the LB samples.

Table 4. Pore Structure Information from Different Methods from the UB and LB Shale at Different CO_2 Exposure Times

	surface area, m^2/g	pore volume, 10^2 cm^3/g	
sample #	BET	BJHAD	BJHDE
UB-0	6.85	2.43	2.38
UB-3	9.31	1.99	1.87
UB-8	10.72	2.06	1.93
UB-16	12.86	2.35	2.21
UB-30	9.01	1.94	1.81
UB-60	3.71	0.78	1.00
LB-0	6.68	3.03	3.07
LB-3	5.57	2.32	2.30
LB-8	6.06	2.22	2.20
LB-16	6.69	1.29	1.57
LB-30	5.75	2.33	2.30
LB-60	4.55	1.92	1.91

2.2. Mineralogical Analysis and TOC. To evaluate mineralogical components, the samples were crushed to a size less than 0.125 mm using a 125 mesh size.[5] For the mineralogical content analysis, a D8 advanced X-ray diffractometer (XRD) was used with a scanning rate of 3°/min in the range of 3−90°. A curve fitting method was used to delineate major minerals (major peaks) that exist in the spectrum. XRD was carried out to measure the changes of mineral composition of the shale samples before and after exposure to $ScCO_2$. For the total organic carbon (TOC) estimation, a Rock-Eval 6 pyrolysis instrument was used under the Shale Play method, a trademark of Institut Français du Pétrole (IFP), where 30 mg of the sample was put into the oven for the analysis. The steps are suggested by Behar et al.[54] to derive the geochemical parameters. The temperature schedule for the Shale Play method was set as follows: the

https://dx.doi.org/10.1021/acs.energyfuels.0c03763
Energy Fuels XXXX, XXX, XXX−XXX

initial temperature was 100 °C, which at 25 °C/min was increased to 200 °C and then kept constant for 3 min (for Sh0 calculations). In the next stage, the temperature was increased at 25 °C/min to 350 °C and held steady for 3 min, and finally, the temperature was increased 25 °C/min to 650 °C. This method resulted in the calculation of all geochemical parameters along with the TOC of the samples: Sh0, Sh1, and Sh2.[3]

2.3. Gas Adsorption. All samples with a particle size less than 250 μm were degassed at 110 °C for a minimum of 8 h to extract moisture and volatiles that might be present in the sample. Low-pressure nitrogen (N_2) adsorption was measured at 77 K/−196.15 °C on a Micromeritics Tristar II device. The amount of gas adsorption was measured over a relative adsorption pressure equilibrium (P/P_0) ranging from 0.01 to 0.99, where P is the system gas vapor pressure and P_0 is the nitrogen saturation pressure.[12] To obtain and interpret PSD curves by the gas adsorption process, the molecular density functional (DFT) and the Barret Joyner and Halenda (BJH) model were adopted.[55,56] The specific surface area (SSA) was estimated using the Brunauer−Emmett−Teller (BET) model under relative pressure (P/P_0) in the range of 0.05 to 0.30.[57] DFT can be used to describe the adsorption and phase behavior of fluids confined in pore structures based on the fundamental principles of statistical mechanics in describing the molecular behavior of confined fluids in pore spaces. Thus, DFT can capture the essential characteristics of the pore spaces filled with fluids and their manifested hysteresis compared to other common techniques. This may contribute to a more accurate evaluation of the curves of pore size distribution over a full range of values (from micropores to mesopores).[3,4,58]

2.4. Fractal Method. Fractal dimension is an important tool for characterizing the properties of complex structures in quantitative terms.[59] Various methods of acquiring pore structure data, i.e., HMIP, SEM, small-angle X-ray diffraction analysis, and isotherms for gas adsorption can be input into fractal dimension analysis.[42,60,61] Several models were developed to measure the fractal dimension of porous media based on the gas adsorption and desorption isotherms.[42,44,60] Fractal dimensions determined by adsorption have proven to be a useful and accurate petrophysical parameter for the depiction and quantification of the pore structure and complex surface of irregular porous solids.[62] A fractal dimension is also an intrinsic function of the surface itself, and the correct measure of the fractal dimension can be calculated by using a theoretical model to process the original data.[62] The FHH model is widely used in the calculation of the fractal dimension and can be defined as

$$\ln(V/V_0) = X(\ln(\ln(P_0/P))) + \text{constant} \quad (1)$$

where V is the volume of the N_2 adsorbed gas at the equilibrium pressure, cm^3/g; V_0 is the adsorption volume, cm^3/g; X is the slope of the $\ln(V)$ vs $\ln[\ln(P_0/P)]$; P is the equilibrium pressure, MPa; and P_0 is the saturation pressure, MPa. One can measure the fractal dimension D from the following equations:

$$D = X + 3 \quad (2)$$

$$D = 3X + 3 \quad (3)$$

In the $3X + 3$ and $X + 3$ models, the former is applied in the capillary condensation method, in which the hysteresis loops begins to build, whereas the latter is applied in the van der Waals force.[43] In this work, eqs 1 and 2 were used to calculate the fractal dimension of shale samples for all stages of CO_2 saturation. Different values of the fractal dimension reflect various characteristics of the pore structure of the shale samples. Typically, the value of fractal dimension D ranges from 2 to 3 and is highly influenced by surface geometrical irregularities and roughness.[63] The closer the D value approaches 3, the more complex and irregular the surfaces are.[43,44,64]

3. RESULTS

3.1. Mineralogy. The kerogen type of the sample is dominantly type II marine, and the TOC value was measured, 13.32 wt % for the UB-0 sample and 14.39 wt % for the LB-0 sample. Moreover, the T_{max} was measured, 449 and 448 °C for the UB-0 and LB-0 samples, respectively, indicating that the samples are in the oil window (mature stage of hydrocarbon generation).

Regarding the sample mineralogy, quartz, pyrite, calcite, dolomite, clay minerals (illite, kaolinite, and chlorite), and others (including biotite and muscovite) are predominant, among which quartz is the most abundant in the LB-0 with 53 and 18.7 wt % in the UB-0 (Table 1). The total clay minerals constitute around 50.5 and 19 wt % in the UB and LB sample, respectively, where, illite is the most abundant clay mineral (Tables 2 and 3). Carbonate minerals (calcite and dolomite) are more abundant in the LB-0 sample (3.0 wt % of calcite and 9 wt % of dolomite) than in the UB-0 sample (3.9 wt % of calcite).

Considering the XRD results for the UB and LB shale samples (Tables 2 and 3), there was an obvious alteration in the compositions of the samples after CO_2 saturation. The alterations in shale mineral compositions may be related to the complex chemical reaction between CO_2 and the minerals. When carbon dioxide is injected into shale, it gets dissolved in water and changes the acid−base equilibrium, which then triggers the dissolution and precipitation of minerals.[1,25,32,65−67] Carbon dioxide dissolves in water to form bicarbonate through eq 4 and dissociates to carbonic acid. Hydrolysis and carbonation reactions may occur in the carbonate and clay minerals in the CO_2−shale interaction. However, according to the reaction equations 4−9, illite and chlorite can be converted into quartz, which could be an explanation to why quartz content (eqs 7 and 8) in the Upper Bakken increased after CO_2 exposure and the clay content decreased.

$$H_2O + CO_2 \leftrightarrow H_2CO_3 \leftrightarrow H^+ + HCO_3^- \quad (4)$$

$$CaCO_{3(calcite)} + 2H^+ \leftrightarrow Ca^{2+} + CO_2 + H_2O \quad (5)$$

$$CaMg(CO_3)_{2(dolomite)} + 4H^+ \rightarrow Ca^{2+} + Mg^{2+} + 2CO_2 + 2H_2O \quad (6)$$

$$\text{illite} + 8H^+ \leftrightarrow 0.6K^+ + 2.3Al^{3+} + 0.25Mg^+ + 3.5SiO_2 + 5H_2O \quad (7)$$

$$\text{chlorite} + 16H^+ \leftrightarrow 5Fe^{2+} + 2.3Al^{3+} + 3SiO_2 + 12H_2O \quad (8)$$

$$\text{quartz} + 4H^+ \leftrightarrow Si^{4+} + H_2O \quad (9)$$

https://dx.doi.org/10.1021/acs.energyfuels.0c03763
Energy Fuels XXXX, XXX, XXX−XXX

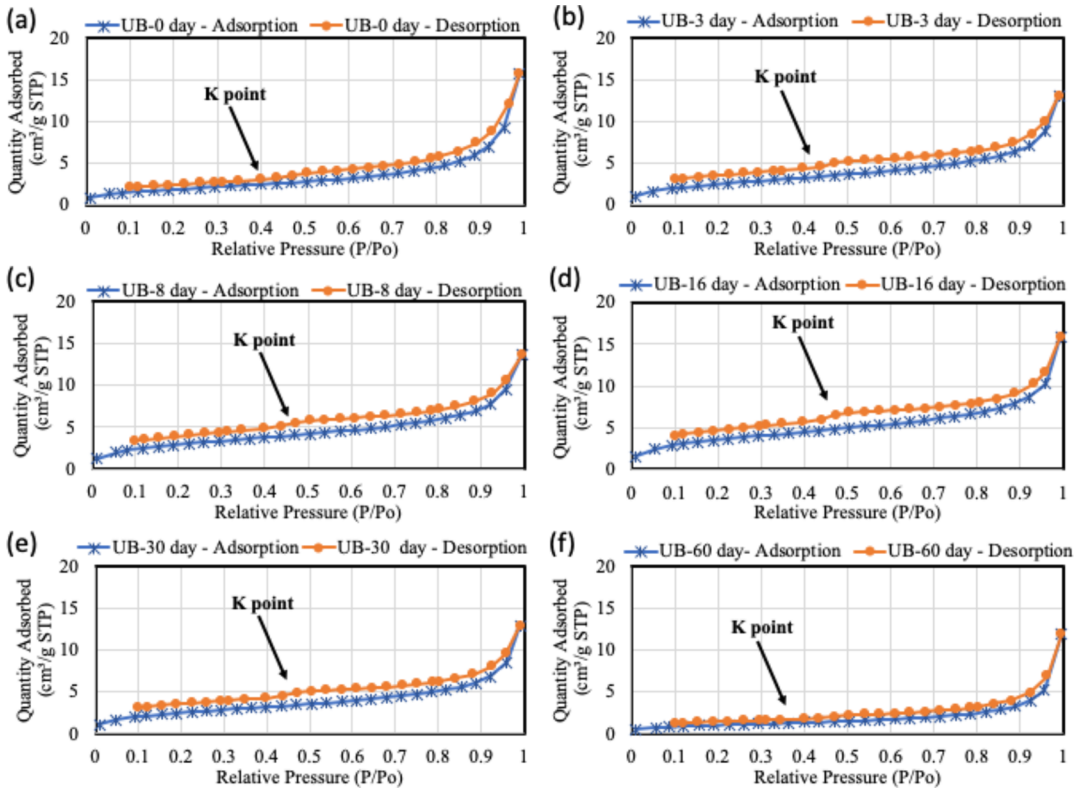

Figure 1. Nitrogen gas adsorption isotherms linear plots of the UB samples before and after CO_2 saturation.

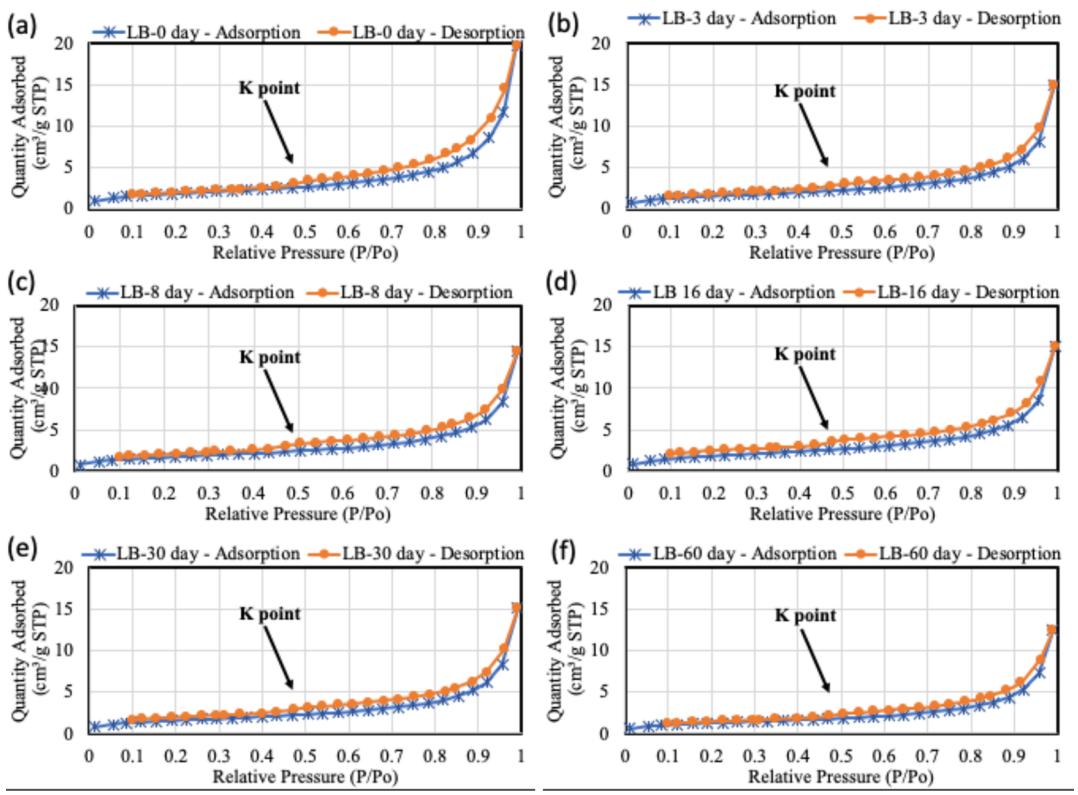

Figure 2. Nitrogen gas adsorption isotherm linear plots of the LB samples before and after CO_2 saturation.

Table 2 summarizes the mineralogical assemblages of the UB sample after each time it was exposed to CO_2. A comparison between the minerals at each stage and prior to CO_2 saturation reveals a clear alteration in mineralogy due to CO_2 exposure. The carbonate minerals are calcite and dolomite, while the clay minerals are illite, chlorite, and kaolinite. It is found that carbonate minerals decreased to various degrees in the UB samples whereas quartz showed an increasing trend. Before

https://dx.doi.org/10.1021/acs.energyfuels.0c03763
Energy Fuels XXXX, XXX, XXX−XXX

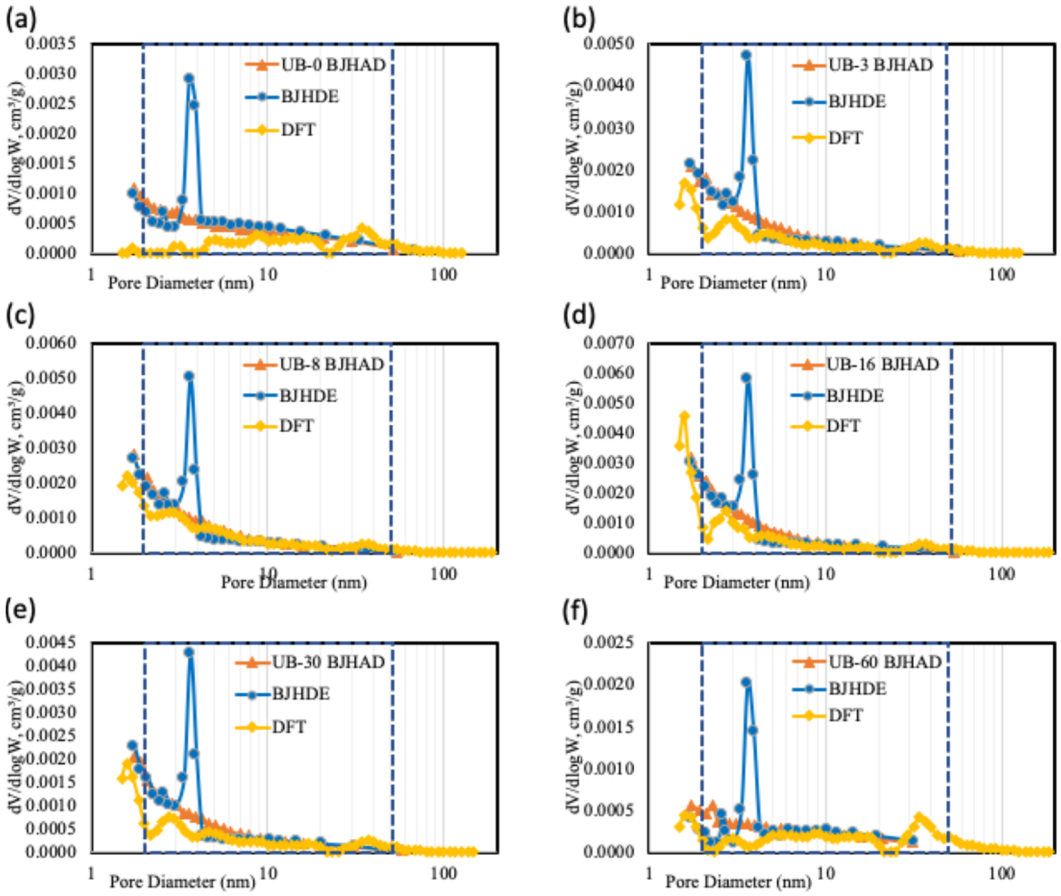

Figure 3. Comparison of the pore size distribution from different methods for the UB for the different stages of CO_2 saturation.

CO_2 saturation, quartz was 18.7 wt % and the exposure resulted in a 24% increase after 3 days, a 33% decrease after 8 days, and a 53% increase after 16 days and remained the same after 30 and 60 days of saturation/exposure from the presaturation value (UB-0). Calcite was 3.9 wt % before saturation, and the exposure caused a 35% increase after 3 days, a 63% decrease after 8 days, a 55% increase after 16 days, a 32.7% decrease after 30 days, and a 51.5% increase after 60 days of CO_2 saturation, compared to the presaturation state. Dolomite was not detected in the UB-0 sample; after 3 days, CO_2 saturation dolomite was detected at 1 wt %, followed by a 68.8% increase after 8 days and a 23.8% increase after 16 days of saturation. Dolomite was not detected after 30 days, and it was at 0.5 wt % after 60 days of CO_2 saturation. The clay minerals at the UB samples were quantified at 50.5 wt % before CO_2 saturation, and their quantity showed a 48.3% decrease after 3 days, a 39.3% increase after 8 days, a 57.7% decrease after 16 days, a 59.3% decrease after 30 days, and a 41.3% increase after 60 days. Collectively, it was observed that the magnitude of changes in mineral assemblages was reduced after 16 days of saturation regardless of the type of mineral.

The mineralogy of the LB sample also changed during the CO_2 saturation (Table 3) compared to the initial condition (LB-0). The clay minerals here are illite, chlorite, and kaolinite. Calcite, dolomite, and quartz decreased and then increased to various degrees in the LB sample at various stages, whereas clay minerals increased and then decreased. The quartz amount was 53 wt % before CO_2 saturation, which showed a 15% decrease after 3 days, a 2% decrease after 8 days, a 25% decrease after 16 days, a 27% increase after 30 days, and a 6% decrease after 60 days of saturation. Calcite was initially measured at 3 wt % before CO_2 saturation, which resulted in a 67% decrease after 3 days of saturation. Calcite was not detected after 8 days, and its quantity changed as follows: 6 wt % after 16 days, followed by a 67% decrease after 30 days, and an 80% increase after 60 days. Dolomite was initially measured at 9 wt % before CO_2 saturation, which then resulted in a 67% decrease after 3 days of saturation, a 9% increase after 8 days of saturation, a 63% increase after 16 days of saturation, a 55% decrease after 39 days of saturation, and a 20% increase after 60 days of saturation. The initial clay minerals' weight percentage was measured at 19%, which was followed by a 24% increase after 3 days, an 8% decrease after 8 days, a 4% decrease after 16 days, a 9% decrease after 30 days, and 12% decrease after 60 days. The breakdown of the clay minerals is shown in Table 3. In general, the clay minerals expressed a decreasing trend, while quartz showed an increasing trend during CO_2 saturation in LB samples.

3.2. Gas Adsorption. The nitrogen adsorption isotherms of 12 samples from both UB and LB samples are displayed in Figures 1 and 2. All the adsorption isotherms displayed similar morphological attributes. During the adsorption process, as the relative pressure increased from 0, the adsorbed gas quantity increased rapidly and then increased monotonically until it reached the maximum relative pressure. Adsorption−desorption isotherm hysteresis loops were also observed in each isotherm for both UB and LB samples before and after CO_2 saturation, which were produced by capillary condensation in

https://dx.doi.org/10.1021/acs.energyfuels.0c03763
Energy Fuels XXXX, XXX, XXX−XXX

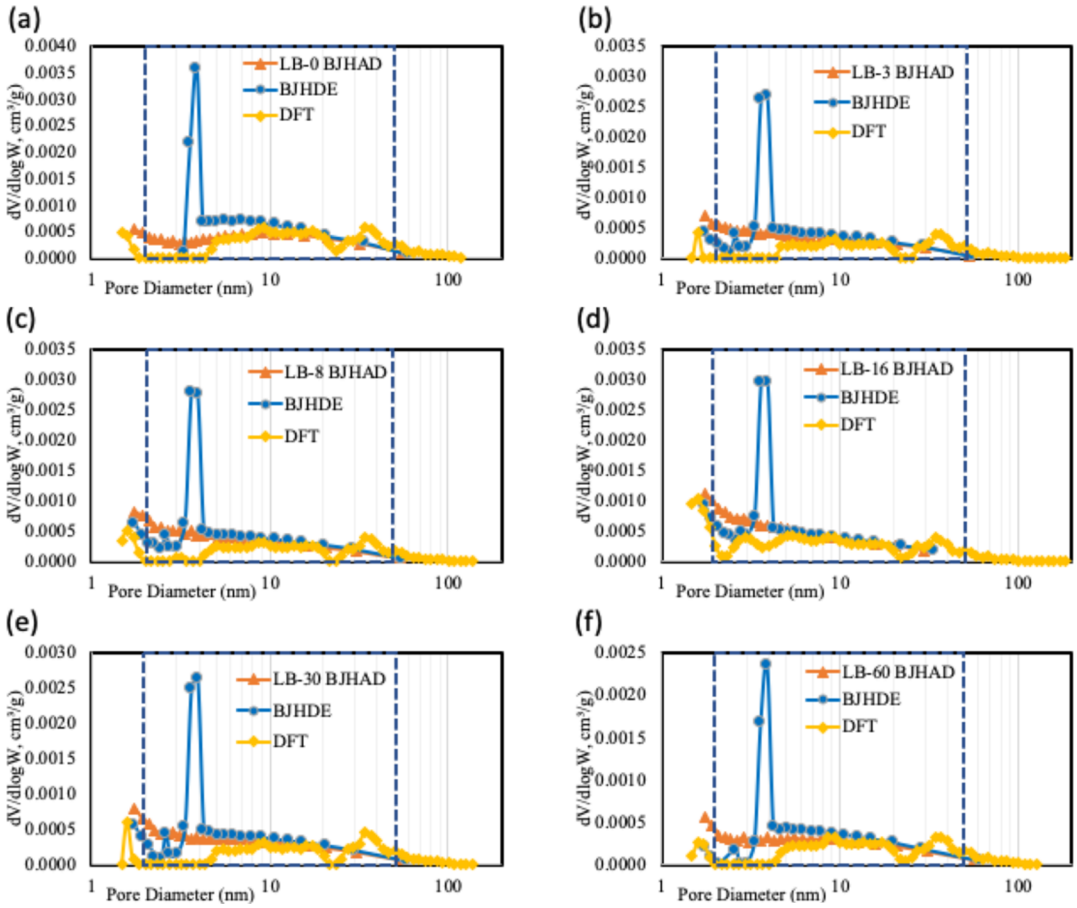

Figure 4. Comparison of the pore size distribution from different methods for the LB for the different stages of CO_2 saturation.

the mesopores of shale.[68] Interestingly, a reflection point known as the *K* point or cavitation is observed in each desorption branch for all the shale samples. Cavitation is a phenomenon in which raid changes of pressure in a liquid lead to the formation of small vapor−filled cavities in places where the pressure is relatively low.[69,70] The P/P_0 corresponding to the *K* point in each desorption branch for all the shale samples is measured to be around 0.5 relative pressure, as also reported by other researchers.[33,69] The rate of gas adsorption increases when the relative pressure is larger than 0.8 until the relative pressure is closer to 1. There is a hysteresis loop in the adsorption−desorption isotherm at a P/P_0 of 0.4−0.99. At a P/P_0 below 0.40, the adsorption curve is almost overlapped with the desorption curve due to the tensile strength effect. As P/P_0 increases, the hysteresis loop occurs, which is either due to the mesopore−macropore capillary condensation or the pore network.

It is observed that the loops remain nearly horizontal and parallel over a wide range of relative pressures (P/P_0), which corresponds to the pore sizes that are present in the samples.[4,71] The shape of the hysteresis loop can be used to determine the morphology of the shale pore structure.[4,71,72] Furthermore, the adsorption isotherms in the samples belong to type IV, and the shape of the pores in the UB and LB samples are mainly narrow slit-like based on the IUPAC category of pore shapes. The adsorbed amount for the UB-0 at the initial stage before CO_2 is 15.7 cm^3/g STP, and after 3 days of saturation the quantity absorbed decreased to 13.1 cm^3/g STP. Following the exposure time, the quantity of absorbed gas for the 8, 16, 30, and 60 days of saturation was 13.6, 15.9, 12.9, and 11.9 cm^3/g STP, respectively (Figure 1a−f). The adsorbed amount for the LB samples also has a trend similar to the UB samples where at the initial stage before CO_2 exposure it was measured as 19.7 cm^3/g STP. After 3 days of saturation, the quantity of absorbed gas decreased to 15.0 cm^3/g STP. The quantity of absorbed gas for the 8, 16, 30, and 60 days was measured to be 14.5, 14.9, 15.1, and 12.5 cm^3/g STP, respectively (Figure 2a−f). The adsorbed amount of nitrogen in the CO_2 saturated samples is smaller than that before saturation (UB-0 and LB-0). CO_2 saturation thus decreased the nitrogen adsorption ability of UB and LB samples primarily because the adsorption capacity is largely controlled by mesopores. As CO_2 dissolves a portion of the pore space, the number of mesopores decreases, as presented, and the adsorption capacity is thus reduced. As seen in Figures 1 and 2, there is only a slight shape difference in the hysteresis loops of isotherms before and after CO_2 saturation for the UB and LB samples. It can be concluded that the interaction of UB and LB to CO_2 has a minor effect on the pore shape of the shale samples in this study.

3.3. Pore Size Distribution (PSD). PSDs are calculated by three different methods for all stages of CO_2 saturation for the UB and LB samples. Results are presented in Figures 3 and 4. The ordinate parameter d*V*/d log *W* is called the log differential pore volume versus diameter.[12] It is understood that each of the BJHAD, BJHDE, and DFT models result in different distribution curves for each sample at the same stage of saturation, and they do not match perfectly. For the DFT

https://dx.doi.org/10.1021/acs.energyfuels.0c03763
Energy Fuels XXXX, XXX, XXX−XXX

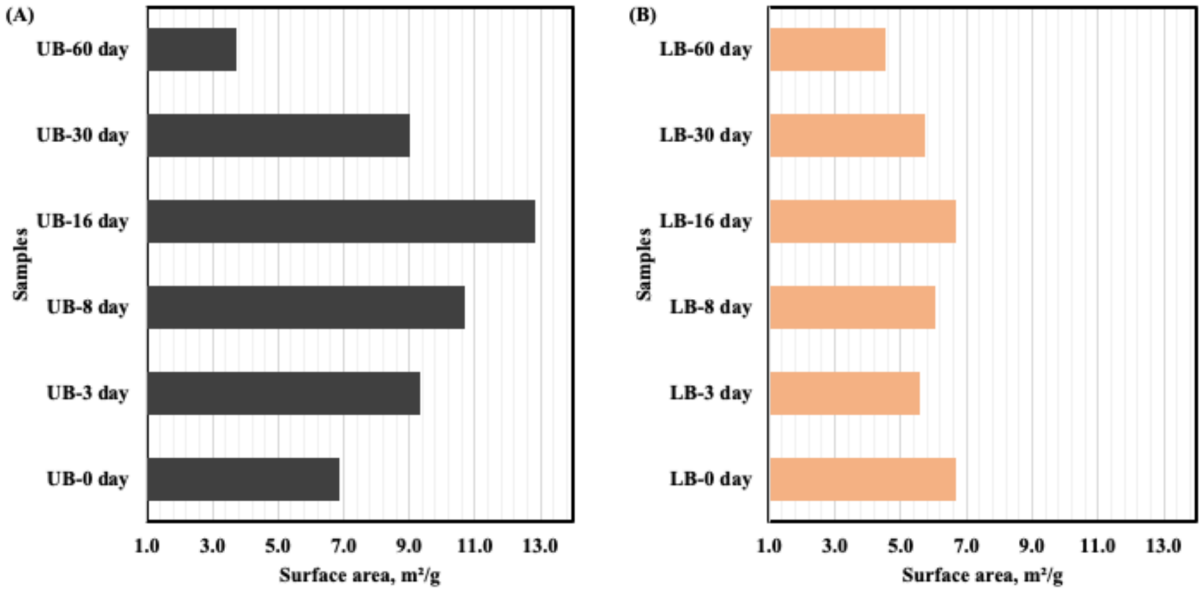

Figure 5. Surface area using the BET method for the (a) UB and (b) LB for the different stages of CO_2 saturation.

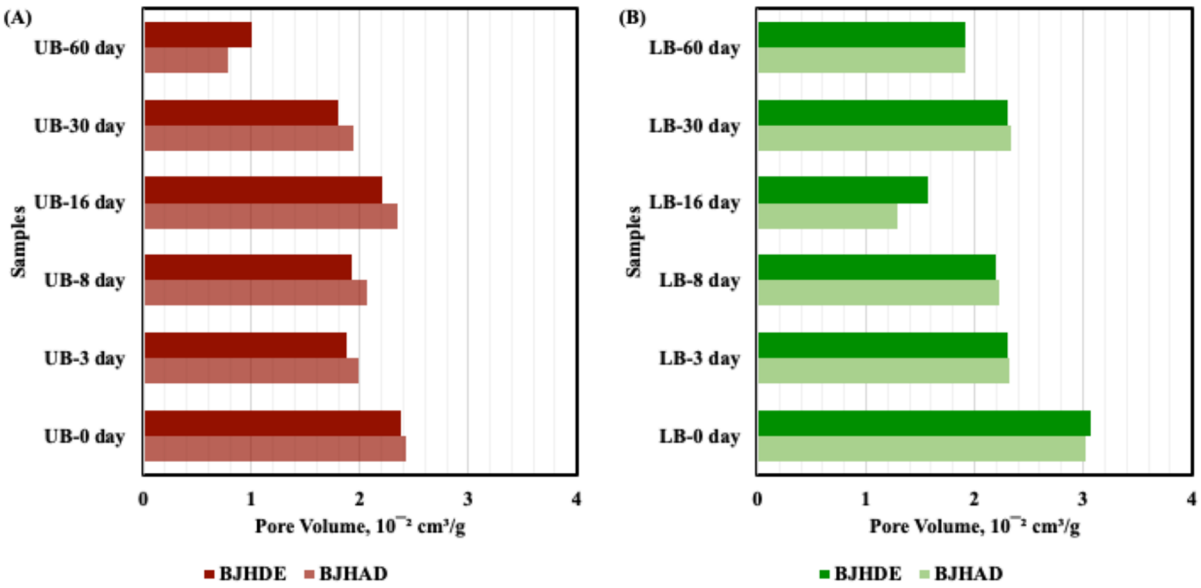

Figure 6. Comparison of the pore volume for the (a) UB and (b) LB shale samples for the different stages of CO_2 saturation.

analysis, we chose the adsorption isotherm for the data input and calculated the pore size distribution based on the carbon surface calculation model. This is based on how each model calculates the PSDs. On the basis of average pore size obtained from adsorption isotherms, it is seen that the average pore diameter of the samples varies from 7.6528 (UB-16) nm to 19.9608 nm (UB-10) and 13.8469 nm (LB-16) to 18.2654 nm (LB-0) in the UB and LB samples, respectively, using the BJHAD model, which falls within the range of mesopores (pores with widths between 2 and 50 nm) based on IUPAC classification of pore sizes.

3.4. Pore Structure Analysis. The main method that was used extensively to quantify the pore structure details is the density functional theory (DFT).[57] The pore structure of the shale samples using the DFT from the isotherms was analyzed and is presented in Figures 3 and 4. The surface area and pore volume of the samples are summarized in Table 4. It is important to note that the phase behavior of fluids in a confined pore can be described using DFT.[73] The PSD of the UB samples before CO_2 saturation using the DFT model and the mesopores (2−50 nm) suggest that the UB-0 exhibits a multimodal characteristic with peaks at 3, 5, 9, and 35 nm. After CO_2 saturation, samples UB-3, UB-30, and UB-60 exhibit a trimodal characteristic with peaks around 3, 6, and 35 nm while UB-8 and UB-16 expressed a bimodal characteristic with peaks at 3 and 35 nm. All the samples from the UB consistently display peaks at 3 and 35 nm. The PSD of the LB sample before CO_2 saturation (LB-0) shows a bimodal characteristic with peaks at 9 and 35 nm. Furthermore, LB-3, LB-8, LB-30, and LB-60 samples also exhibit a bimodal characteristic with peaks at 9 and 35 nm after CO_2 saturation, whereas sample LB-16 has multimodal characteristics with peaks at 3, 5, 9, and 35 nm. All of the samples from the LB samples show peaks at 9 and 35 nm. The PSD trends that were recorded in this study

https://dx.doi.org/10.1021/acs.energyfuels.0c03763
Energy Fuels XXXX, XXX, XXX−XXX

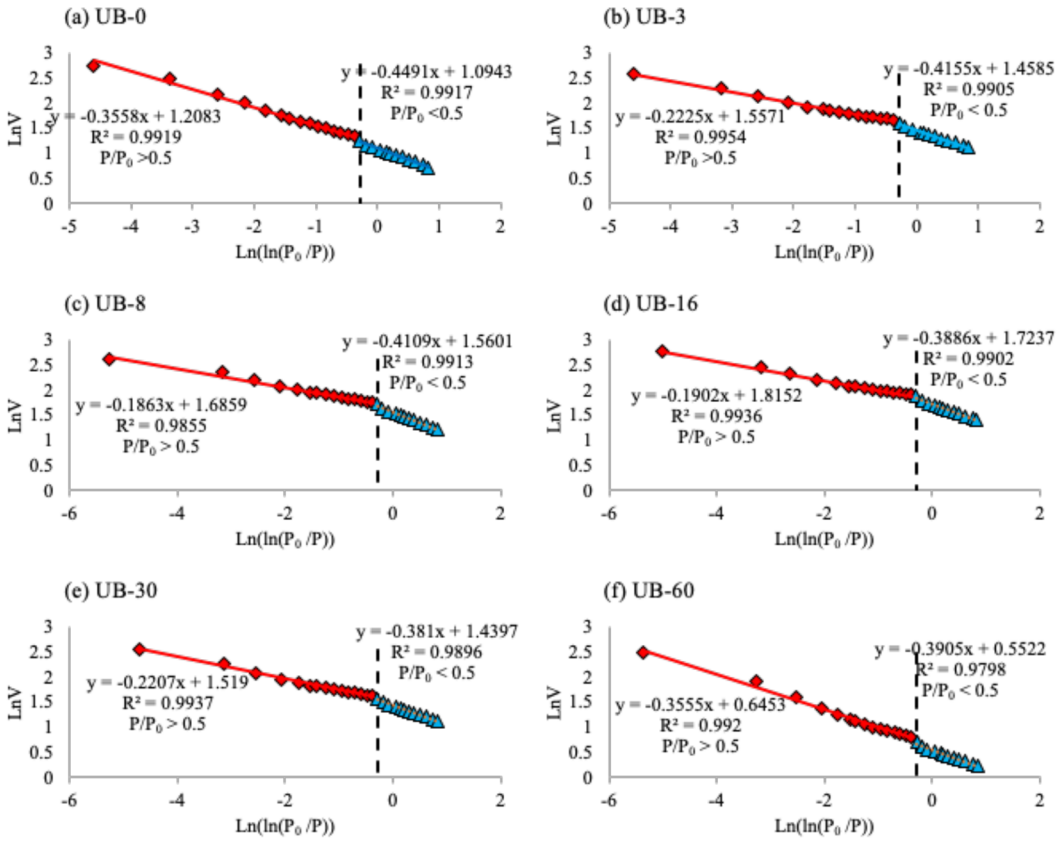

Figure 7. Fractal analyses of the UB samples before and after saturation based on nitrogen gas desorption isotherms.

on the UB and LB samples through exposure have also been observed and reported by other researchers.[14]

3.5. The Surface Area. The surface area of pores surveyed in the samples varies from 3.71 m^2/g to 12.86 m^2/g and 4.55 m^2/g to 6.69 m^2/g for the UB and LB shale samples, respectively (Figure 5). The surface area was determined using the BET model for both the UB and LB shale samples. Before CO_2 saturation, the surface area for the UB was 6.85 m^2/g; after 3 days of saturation, the surface area increased to 9.31 m^2/g and continued on the increasing trend with a peak at 12.86 m^2/g after 16 days of saturation. The surface area then decreased to 9.01 and 3.71 m^2/g after 30 and 60 days of saturation, respectively. Before CO_2 saturation, the area for the LB was 6.68 m^2/g, while after 3 days of saturation the surface area decreased to 5.57 m^2/g, started to increase after 8 days of saturation, and continued to increase with a peak at 6.69 m^2/g after 16 days of saturation. The surface area then decreased to 5.75 and 4.55 m^2/g after 30 and 60 days of saturation, respectively. The pore surface area of the shale observed from the UB sample is larger than the surface area of the LB samples (Table 4).

3.6. The Pore Size and Pore Volume. The pore size and the pore volume of the shale samples was determined from the BJH adsorption (BJHAD) and the BJH desorption (BJHDE) model.

Considering the pore volume of the UB sample, before CO_2 saturation as Table 4, Figure 6a illustrate, it was quantified as 2.40×10^{-2} cm^3/g. Furthermore, inspecting UB-3, the pore volume decreased to 1.93×10^{-2} cm^3/g and then increased to 1.99×10^{-2} cm^3/g for UB-8 and peaked at 2.28×10^{-2} cm^3/g in the UB-16 sample. Finally, the peak of the pore volume in UB-16 decreased to 1.87×10^{-2} cm^3/g and 0.89×10^{-2} cm^3/g in UB-30 and UB-60 samples, respectively. The same analysis and calculations on the LB samples denoted that the pore volume of the LB sample before getting exposed to the CO_2 was estimated as 3.05×10^{-2} cm^3/g, as can be seen in Table 4 and Figure 6b. Following the exposure time series, the LB-3 sample's pore volume decreased to 2.31×10^{-2} cm^3/g and then to 2.21×10^{-2} cm^3/g and, finally, to 1.43×10^{-2} cm^3/g in the LB-8 and LB-16 samples. Ultimately, the pore volume increased to 2.32×10^{-2} cm^3/g in the LB-30 sample and decreased to 1.92×10^{-2} cm^3/g after 60 days of exposure.

Unpredictability can emerge in hierarchical frameworks contained both micro−mesopores that makes a more extensive assortment in the observed hysteretic conduct. This unpredictability is characteristic of the adsorbed liquid and encompassing pore framework and can veil occurrences like the pore blocking and cavitation coming from the desorption isotherm. This will confuse matters from the perspective of characterization. In any case, if the hysteresis loop is deciphered accurately, it can give a bunch of data about the pore network morphology. In the case of cavitation, the pore size is clouded, as the point of desorption is feebly related with the pore size. Cavitation happens during the desorption cycle coming about because of the unconstrained nucleation and development of gas rises in the metastable liquid restricted in the pores. A sustained metastable state of the concentrated fluid that is overstretched by capillary pressure includes the mechanism leading up to this spontaneous act. It is generally associated with spherical pore systems linked by smaller necks as shown in Figures 1 and 2.

https://dx.doi.org/10.1021/acs.energyfuels.0c03763
Energy Fuels XXXX, XXX, XXX−XXX

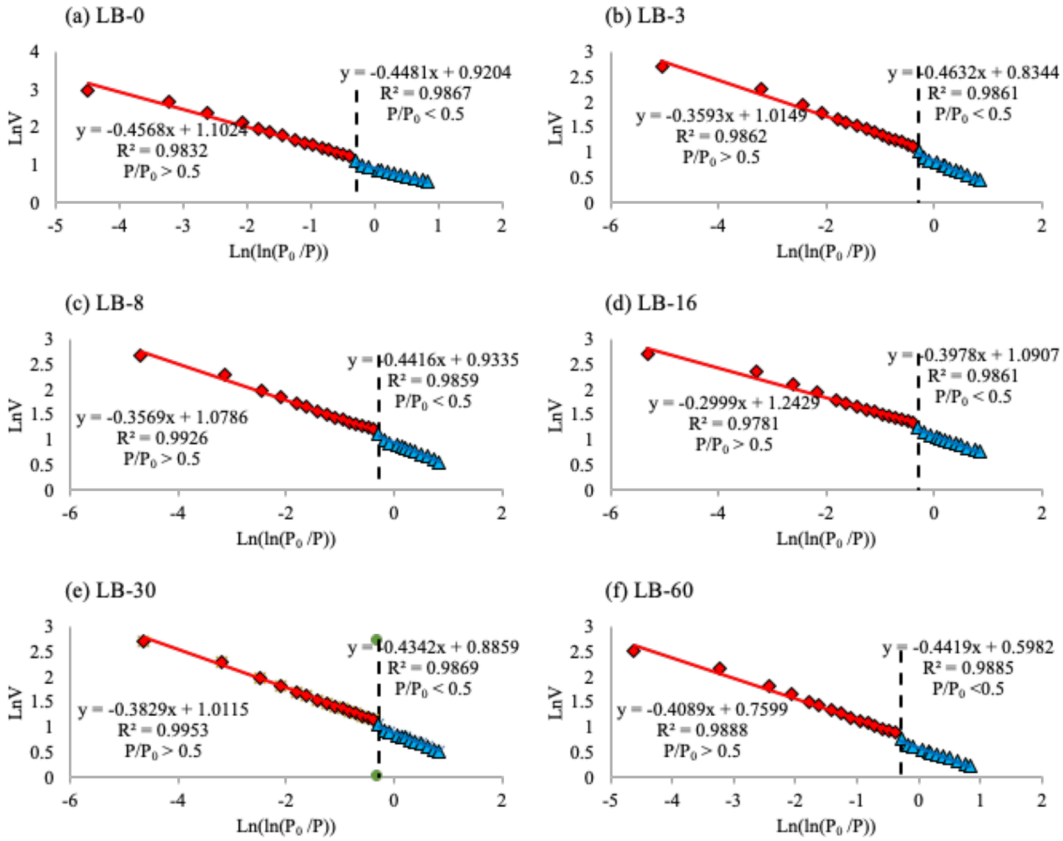

Figure 8. Fractal analyses of the LB samples before and after saturation based on nitrogen gas desorption isotherms.

Table 5. Fractal Dimensions Determined by the FHH Model Based on Nitrogen Gas Desorption Isotherm for the UB and LB Samples

	P/P_0: 0−0.5			P/P_0: 0.5−1.0		
sample #	X_1	$D_1 = 3 + X_1$	R^2	X_2	$D_2 = 3 + X_2$	R^2
UB-0	−0.4491	2.5509	0.9917	−0.3558	2.6442	0.9919
UB-3	−0.4155	2.5845	0.9905	−0.2225	2.7775	0.9954
UB-8	−0.4109	2.5891	0.9913	−0.1863	2.8137	0.9855
UB-16	−0.3886	2.6114	0.9902	−0.1902	2.8098	0.9936
UB-30	−0.381	2.619	0.9896	−0.2207	2.7793	0.9937
UB-60	−0.3905	2.6095	0.9798	−0.3555	2.6445	0.992
LB-0	−0.4481	2.5519	0.9867	−0.4568	2.5432	0.9832
LB-3	−0.4632	2.5368	0.9861	−0.3593	2.6407	0.9862
LB-8	−0.4416	2.5584	0.9859	−0.3569	2.6431	0.9926
LB-16	−0.3978	2.6022	0.9861	−0.2999	2.7001	0.9781
LB-30	−0.4342	2.5658	0.9869	−0.3829	2.6171	0.9953
LB-60	−0.4419	2.5581	0.9885	−0.4089	2.5911	0.9888

3.7. Fractal Dimensions from Gas Adsorption Experiment. Fractal dimensions were determined on the basis of the N_2 desorption isotherm data and FHH fractal model. Figures 7 and 8 display the plots of $\ln(V)$ vs $\ln(\ln(P_0/P))$ from the UB and LB shale samples before and after CO_2 saturation. The fractal dimension can be obtained from the slope of the fitting curve. From linear segments at P/P_0, the fractal dimension D_1 was determined in the range 0−0.5, while D_2 was determined from the linear segments at P/P_0 in the range of 0.5−1.0. Fractal dimension values of all the UB and LB shale samples before and after CO_2 saturation are listed in Table 5. The D_1 and D_2 values for the UB samples are in the ranges of 2.5509−2.619 (average, 2.5941) and 2.6442−2.8137 (average, 2.7448), respectively. The D_1 and D_2 values for the LB samples are in the range of 2.5599−2.6022 (average, 2.5622) and 2.5432−2.7001 (average, 2.6226), respectively. The correlation coefficients, R^2, of the samples before and after CO_2 saturation are larger than 0.9, suggesting that the UB and LB samples have obvious strong fractal characteristics. In previous studies, the significance of D_1 and D_2 was identified, in which D_1 reflects the roughness of the shale surface, while D_2 is used to quantitatively describe the irregularity and heterogeneity of the pore structure.[42,74]

The fractal dimension increased as samples were saturated with CO_2 with the peak fractal dimension at 8 days and 16 days and decreased at 30 days and 60 days for both the UB and

https://dx.doi.org/10.1021/acs.energyfuels.0c03763
Energy Fuels XXXX, XXX, XXX−XXX

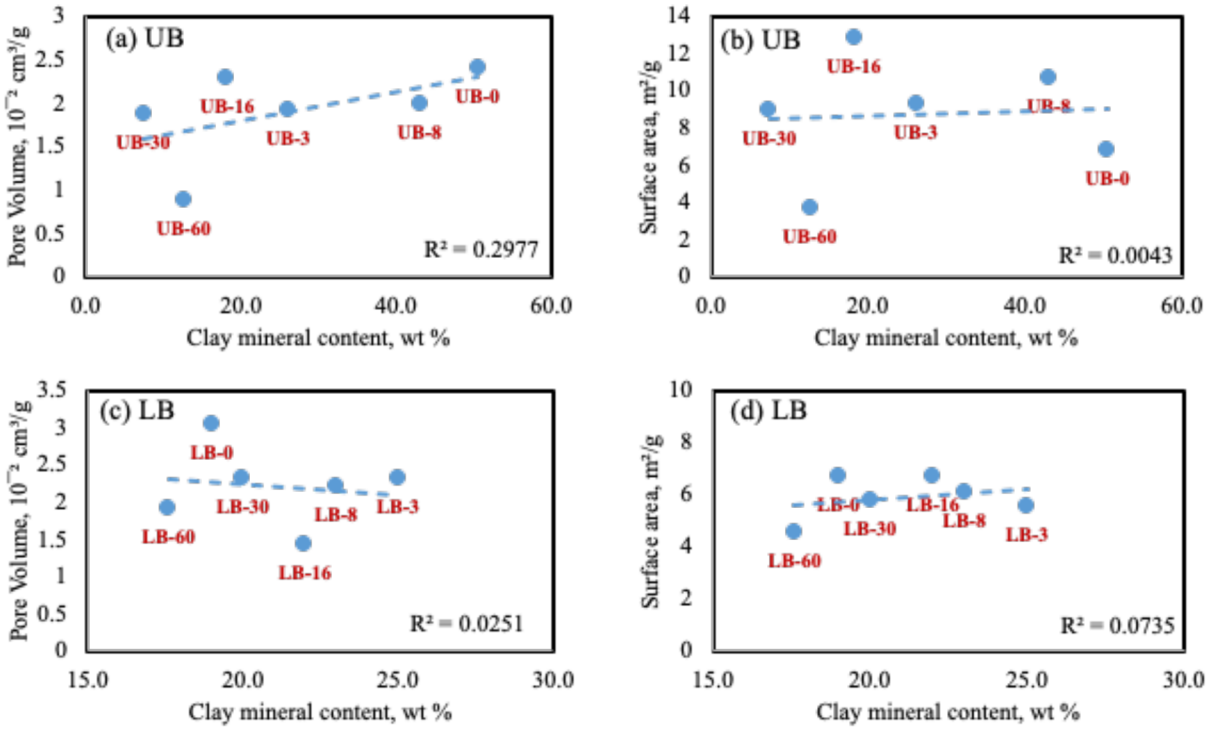

Figure 9. Interrelationship between the pore structure parameters of UB and LB shale samples before and after CO_2 saturation. (a) Pore volume of UB shale versus clay mineral content. (b) Specific surface area of UB shale versus clay mineral content. (c) Pore volume of LB shale versus clay. (d) Specific surface area of LB shale versus clay mineral content.

LB samples. This suggests an increase in the roughness degree of the shale geometrical surfaces and in the morphology of the pore structure being transformed gradually from regular to complex and back to homogeneity after 60 days of saturation. Therefore, the samples developed a complex pore internal structure and irregular and rough pore surfaces after CO_2 saturation. In addition, the fractal dimension also increased with increasing P/P_0, suggesting that D_2 is larger than D_1 for both UB and LB samples.

4. DISCUSSION

4.1. Chemistry Controls on Shale Pore Structure. The relationships between the shale mineral composition, exposure of the shale material to CO_2, and how the changes affect the pore structure of the material using N_2 gas adsorption are discussed. The correlations between mineralogical composition and TOC content on one hand and the length of CO_2 saturation in days on the other hand were investigated. Previous studies on the controlling factor of shale pore structure have been performed, most of which indicate that TOC and mineral composition are the key factors for PV and SSA variations.[33,34,41,42] Previous studies suggest that organic matter plays an active role in the development of pore systems in shales. The correlation of PV and SSA with TOC is beyond the scope of this study because TOC for this experiment was only measured for UB-0 and LB-0. The variations in mineral composition are attributed to the physicochemical activity of the CO_2 with carbonates and clay minerals that are dissolved in an acid and high-pressure environment. The clay mineral content effects on pore structure are plotted in Figure 9. The regression analysis performed on the UB (Figure 9a,b) and LB shale samples showed that both the PV and SSA possess a weak positive linear correlation as the number of CO_2 saturation days increases, while the SSA versus clay mineral content of the LB shale sample (Figure 9c, d) showed a weak negative linear correlation as the number of CO_2 saturation days increased. This result shows that clay minerals can influence the development of shale pore structure, particularly for the mesopore in this context, which is primarily based on the contribution of illite to the development of the pores.[42]

Clays and carbonates are common mineral components that can get dissolved in the presence of weak acid conditions or by CO_2 exposure. This dissolution of clay and carbonate minerals increased pore spaces and improved the connectivity of the pore structures, as has been also reported by other researchers.[14,75,76] The UB shale sample has larger quantities of clay minerals and carbonates compared to the LB one, while the LB shale sample contains more quartz. This explains why the LB sample has a larger pore volume and pore sizes as a result of the exposure to CO_2 causing the dissolution of the clay minerals and carbonates. Comparing the mineralogical assemblages and resultant time of exposure with the gas adsorption data analysis, the LB sample demonstrated a higher frequency of various pore sizes, larger pore volumes, and larger potential for the adsorption of the gas, as shown in Figures 1 and 2, than the UB sample. On the other hand, surface area (Table 4) was estimated to be larger in the UB sample than in the LB shale sample. Larger adsorption capacity in the LB sample was to some extent related to the pore sizes, pore volume, mineral composition, and TOC of the sample.[33,41,42] Expectations from previous studies is that those samples with larger TOCs should have a larger clay mineral content in the shale samples, which is not the case in this study of the LB shale sample having more TOC but less clay minerals. Carbonate dissolution will increase the pore size of the shale samples, so the dissolution of carbonate exhibits a positive

https://dx.doi.org/10.1021/acs.energyfuels.0c03763
Energy Fuels XXXX, XXX, XXX−XXX

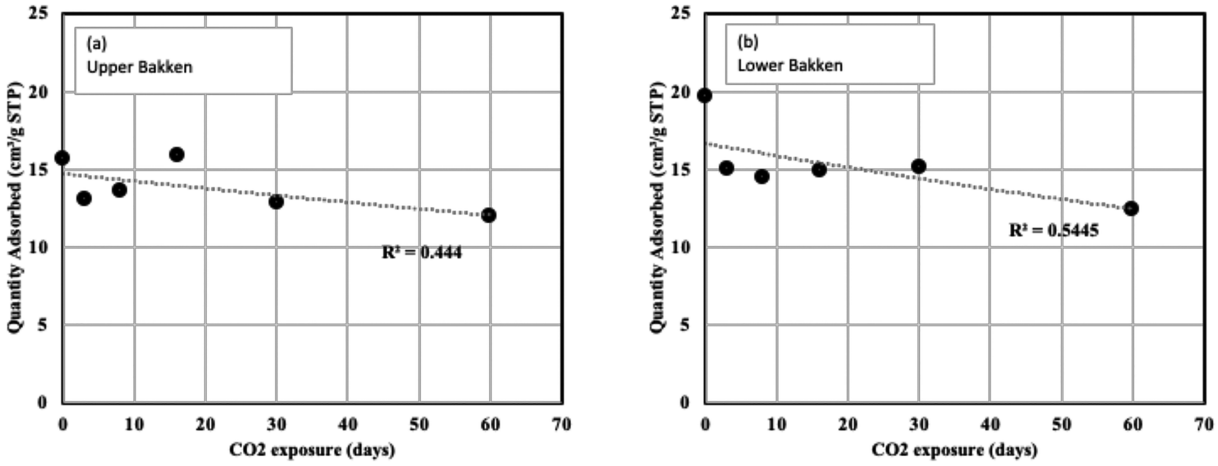

Figure 10. Relationship between the quantity of gas adsorbed versus the length of CO_2 exposure in days.

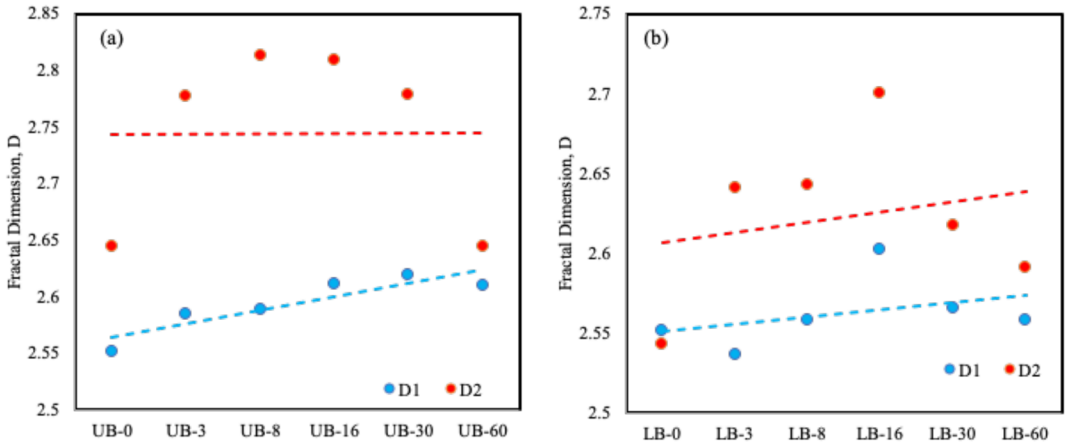

Figure 11. Variation of fractal dimension of shale samples before and after CO_2 saturation from N_2 gas adsorption: (a) UB samples and (b) LB samples.

relationship with the increase in pore volume and the overall adsorption potential of the samples.

The larger pore size, pore volume, and quartz that were recorded in the LB shale sample have resulted in a larger gas adsorption quantity (Figure 10) before and even after CO_2 saturation. It is also observed that the gas adsorption quantity for both the UB (Figure 10a) and the LB (Figure 10b) samples reached a value of about 12 cm^3/g STP after UB-60 and LB-60.

4.2. Correlation between Pore Structure Parameters and Fractal Dimensions. The pore structure parameters and fractal dimensions (both D_1 and D_2) relationships were investigated as well to provide a better insight into the observed changes. The fractal dimensions (Figure 11) show a variation of fractal dimension in shale for the UB and LB samples before and after CO_2 saturation. It can be seen that the D_1 and D_2 of the UB shale (Figure 11a) increased after CO_2 saturation and the D_1 peak at UB-8 and the fractal dimension decreased, while D_2 peaked at UB-30 and the fractal dimension decreased. The D_1 of the LB shale sample decreased after CO_2 saturation in LB-3 and increased for LB-8 and LB-16, while the fractal dimension then decreased for LB-30 and LB-60. Furthermore, D_2 displayed an increasing trend after CO_2 saturation with the peak at LB-16 and the fractal dimension decreased for LB-30 and LB-60 (Figure 11b). The D_1 and D_2 behavior of the UB and LB indicated that the roughness of the pore surface and the complexity of pore structure in shale were increased after 8−16 days of CO_2 saturation, and the complexity and roughness decreased after 30−60 days of CO_2 saturation, which was reported by other researchers.[34]

The increasing and decreasing trends of D_1 and D_2 of the UB and LB shale after CO_2 saturation is mainly the result of the combined effects of dissolution or precipitation and the CO_2-adsorption induced swelling, which correlates with the variations in the pore structures.[33,34,77,78] Previous studies have shown that D_1 has a positive correlation with specific surface area and that D_2 has a negative correlation with the average pore size.[14,34] The dissolution of organic matter or clay minerals in the shale after CO_2 saturation causes some of the micropores to disappear and convert into meso- and macropores, thereby increasing and decreasing specific surface area and D_1.[42] On the basis of our results, it is important to note that interpreting D_2 variations is somehow complicated and requires further studies. On the basis of the following figures, we were not able to draw a robust conclusion as to how the D_2 is changing throughout the experiments.

As illustrated in Figure 12, the relationships between pore structure parameters and fractal dimension (both D_1 and D_2) were investigated. The fractal dimension D_1 for UB shale

https://dx.doi.org/10.1021/acs.energyfuels.0c03763
Energy Fuels XXXX, XXX, XXX−XXX

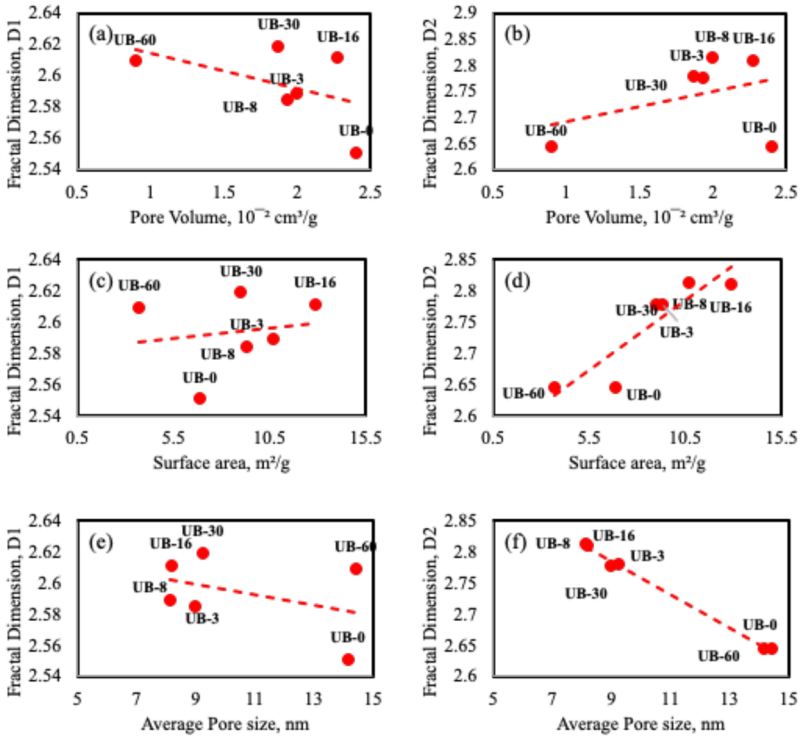

Figure 12. Relationships between fractal dimensions and PV (a, b), SSA (c, d), and average pore width (e, f) for UB shale.

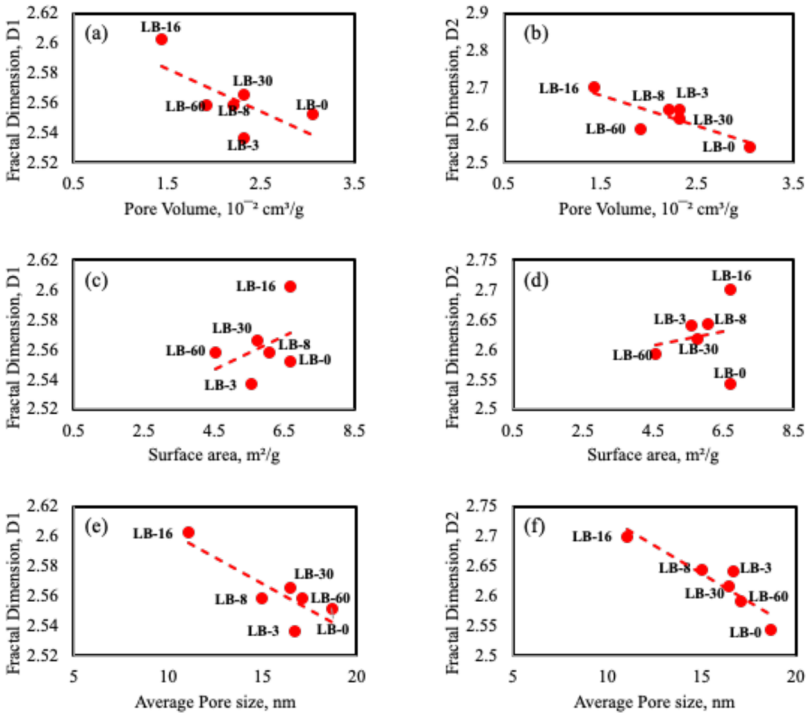

Figure 13. Relationships between fractal dimensions and PV (a, b), SSA (c, d), and average pore width (e, f) for LB shale.

samples has a negative correlation with the total PV (Figure 12a), suggesting that as shale is saturated with CO_2, the fractal dimension D_1 increases with decreasing pore volume. The fractal dimension D_2 has a positive correlation with the PV (Figure 12b), signifying that as the shale is saturated with CO_2, the fractal dimension D_2 decreases with the PV decreasing. The fractal dimensions (both D_1 and D_2) have a positive correlation with the SSA (Figure 12c,d), suggesting that the fractal dimensions increase with the SSA increasing. The result is consistent with previous studies on marine shale.[42] The fractal dimensions (both D_1 and D_2) have a negative correlation with the average pore size (Figure 12e,f) meaning that the fractal dimensions increase when the average pore size is decreased. Figure 13 shows the relationship between pore structure parameters and fractal dimension (both D_1 and D_2). The fractal dimensions (both D_1 and D_2) for LB shale samples have

https://dx.doi.org/10.1021/acs.energyfuels.0c03763
Energy Fuels XXXX, XXX, XXX−XXX

a negative correlation with the total PV (Figure 13), inferring that as shale is saturated with CO_2, the fractal dimensions D_1 and D_2 increase with decreasing pore volume. The fractal dimensions (both D_1 and D_2) have a positive relationship with the SSA (Figure 13c,d). This shows that as the shale is saturated with CO_2, the fractal dimensions increase with the SSA increasing. The fractal dimensions (both D_1 and D_2) have a negative connectivity with the average pore size (Figure 13e,f), which indicates that the fractal dimensions increase as the average pore size is decreasing.

After CO_2 exposure, a significant decrease in the surface area of shales will weaken the gas adsorption capacity as seen in the UB samples, while the increase in larger pores can enhance the pore connection and provide more flow conduit, which will ultimately expect to promote the matrix permeability in the shale formation, also observed in previous literature.[14] Although, the feasibility of storing CO_2 in shale with enhanced hydrocarbon production has been proven by recent field practices.[8] It is important to emphasize that, as research in this area is expanding, there exist many fundamental issues associated with this process. These issues result mainly from the chemical and structural changes in shales, which might affect the stability of the shale reservoir for long-term CO_2 storage.

5. CONCLUSIONS

Samples retrieved from the Upper and Lower Bakken Shale where exposed to CO_2 at different day intervals, to determine the effect that super critical CO_2 storage has on the mineral composition, pore structure, and pore connectivity of the shale. In order to do so, XRD and gas adsorption tests were carried out on the samples at the different saturation stages. On the basis of the research, the following conclusions were made:

1. XRD analysis revealed similar minerals present in the UB and LB samples with varying weight ratios, with quartz being the highest mineral present followed by clay minerals. Clay and quartz generally had an increasing trend related to the days of CO_2 exposure more than other minerals in the samples. The UB shale sample had larger quantities of clay minerals and carbonates compared to the LB shale, while the LB shale sample contained more quartz. Clay minerals can influence the development of shale pore structure, particularly the micropores and mesopores, which is primarily the result of the contribution of illite to the development of the pores. The presence of quartz seems to be playing a role in the pore size structure of the shale samples. The larger the quartz content, the smaller the pore size, as seen in sample UB-8.

2. The dissolution of organic matter or clay minerals in the shale after CO_2 saturation causes some of the pores to disappear or convert, thereby increasing and decreasing specific surface area.

3. Pore surface area using the BET model showed an increasing trend with a peak at after 16 days of CO_2 saturation and then decreased for both the UB and LB samples. The pore volume using the BJH adsorption and desorption model (BJHAD and BJHDE) showed a decreasing trend as the samples were saturated with CO_2 for both UB and LB samples. Surface area is larger in the sample with the larger total organic content.

4. The FHH model can be applied to determine the fractal characteristics of UB and LB shale samples. The fractal dimension increased as samples were saturated with CO_2 with a peak fractal dimension at 8 days and 16 days and decreased at 30 days and 60 days for both the UB and LB samples. This suggests an increase in the roughness degree of the shale geometrical surface and the morphology of the pore structure, which is transformed gradually from regular to complex and back to more homogeneous after 60 days of saturation.

■ AUTHOR INFORMATION

Corresponding Author

Mehdi Ostadhassan − *Key Laboratory of Continental Shale Hydrocarbon Accumulation and Efficient Development, Ministry of Education, Northeast Petroleum University, Daqing 163318, China;* orcid.org/0000-0001-9235-4399; Email: mehdi.ostadhassan@nepu.edu.cn

Authors

Ogochukwu Ozotta − *Petroleum Engineering Department, University of North Dakota, Grand Forks, North Dakota 58203, United States*

Kouqi Liu − *State Key Laboratory of Petroleum Resources and Prospecting and College of Geosciences, China University of Petroleum (Beijing), Beijing 102249, China; Department of Earth and Atmospheric Sciences, Central Michigan University, Mount Pleasant, Michigan 48859, United States*

Thomas Gentzis − *Core Laboratories, Reservoir Geology Group, Houston, Texas 77040, United States*

Humberto Carvajal-Ortiz − *Core Laboratories, Reservoir Geology Group, Houston, Texas 77040, United States*

Bo Liu − *Key Laboratory of Continental Shale Hydrocarbon Accumulation and Efficient Development, Ministry of Education, Northeast Petroleum University, Daqing 163318, China*

Saeed Rafieepour − *McDougall School of Petroleum Engineering, University of Tulsa, Tulsa, Oklahoma 74104, United States*

Complete contact information is available at: https://pubs.acs.org/10.1021/acs.energyfuels.0c03763

Notes

The authors declare no competing financial interest.

■ ACKNOWLEDGMENTS

The authors wish to acknowledge the North Dakota Industrial commission for their financial support for this research. The authors wish to thank North Dakota Geological Survey, Core Library, for giving us access to the Bakken core samples, particularly Jeffrey Bader, geologist and director, as well as Kent Hollands, lab technician. The authors would also like to express their appreciation to the two anonymous reviewers and editor for constructive comments and reviews, which highly improved the quality of the manuscript.

■ REFERENCES

(1) Zhang, S.; Xian, X.; Zhou, J.; Zhang, L. Mechanical behaviour of Longmaxi black shale saturated with different fluids: An experimental study. *RSC Adv.* **2017**, *7*, 42946−55.

(2) Ostadhassan, M. M. *Geomechanics and Elastic Anisotropy of the Bakken Formation*; Theses and Dissertations, University of North Dakota, Williston Basin, 2013.

(3) Liu, K.; Ostadhassan, M.; Zou, J.; Gentzis, T.; Rezaee, R.; Bubach, B.; et al. Multifractal analysis of gas adsorption isotherms for pore structure characterization of the Bakken Shale. *Fuel* **2018**, *219*, 296−311.

(4) Thommes, M.; Kaneko, K.; Neimark, A. V.; Olivier, J. P.; Rodriguez-Reinoso, F.; Rouquerol, J.; et al. Physisorption of gases,

with special reference to the evaluation of surface area and pore size distribution (IUPAC Technical Report). *Pure Appl. Chem.* **2015**, *87*, 1051−69.

(5) Kuila, U.; Prasad, M. Application of nitrogen gas-adsorption technique for characterization of pore structure of mudrocks. *Leading Edge* **2013**, *32*, 1478−85.

(6) Sorensen, J. A.; Braunberger, J. R.; Liu, G.; Smith, S. A.; Klenner, R. C. L.; Steadman, E. N.; et al. CO_2 storage and utilization in tight hydrocarbon-bearing formations: A case study of the bakken formation in the williston basin. *Energy Procedia* **2014**, *63*, 7852−60.

(7) Jin, L.; Hawthorne, S.; Sorensen, J.; Pekot, L.; Kurz, B.; Smith, S.; et al. Advancing CO_2 enhanced oil recovery and storage in unconventional oil play—Experimental studies on Bakken shales. *Appl. Energy* **2017**, *208*, 171−83.

(8) Sorensen, J.; Jacobson, L.; Pekot, L.; Torres, J.; Jin, L.; Hamling, J.; et al. *Bakken CO_2 Storage and Enhanced Recovery Program*; U.S. Department of Energy, 2017.

(9) Duncan, D. C.; Swanson, V. E. Organic-rich shale of the United States and world land areas. *USGS Circular 523* **1966**, *U.S. Geological Survey*, 30.

(10) Liu, K.; Ostadhassan, M.; Cai, J. *Characterizing Pore Size Distributions of Shale* **2012**, *12*, 93−97.

(11) Huang, X.; Zhao, Y. P. Characterization of pore structure, gas adsorption, and spontaneous imbibition in shale gas reservoirs. *J. Pet. Sci. Eng.* **2017**, *159*, 197−204.

(12) Liu, K.; Ostadhassan, M.; Zhou, J.; Gentzis, T.; Rezaee, R. Nanoscale pore structure characterization of the Bakken shale in the USA. *Fuel* **2017**, *209*, 567−78.

(13) Gao, Z.; Hu, Q. Estimating permeability using median pore-throat radius obtained from mercury intrusion porosimetry. *Journal of Geophysics and Engineering* **2013**, *10*, 025014.

(14) Pan, Y.; Hui, D.; Luo, P.; Zhang, Y.; Zhang, L.; Sun, L. Influences of subcritical and supercritical CO 2 treatment on the pore structure characteristics of marine and terrestrial shales. *Journal of CO_2 Utilization* **2018**, *28*, 152−67.

(15) Clarkson, C. R.; Solano, N.; Bustin, R. M.; Bustin, A. M. M.; Chalmers, G. R. L.; He, L.; et al. Pore structure characterization of North American shale gas reservoirs using USANS/SANS, gas adsorption, and mercury intrusion. *Fuel* **2013**, *103*, 606−16.

(16) Zhao, P.; Wang, Z.; Sun, Z.; Cai, J.; Wang, L. Investigation on the pore structure and multifractal characteristics of tight oil reservoirs using NMR measurements: Permian Lucaogou Formation in Jimusaer Sag, Junggar Basin. *Mar. Pet. Geol.* **2017**, *86*, 1067−81.

(17) Loucks, R. G.; Reed, R. M.; Ruppel, S. C.; Jarvie, D. M. Morphology, Genesis, and Distribution of Nanometer-Scale Pores in Siliceous Mudstones of the Mississippian Barnett Shale. *J. Sediment. Res.* **2009**, *79*, 848−61.

(18) Klaver, J.; Desbois, G.; Urai, J. L.; Littke, R. BIB-SEM study of the pore space morphology in early mature Posidonia Shale from the Hils area, Germany. *Int. J. Coal Geol.* **2012**, *103*, 12−25.

(19) Javadpour, F. Nanopores and apparent permeability of gas flow in mudrocks (shales and siltstone). *Journal of Canadian Petroleum Technology* **2009**, *48*, 16−21.

(20) Liu, K.; Ostadhassan, M.; Bubach, B. *Pore Structure Analysis by Using Atomic Force Microscopy*; Unconventional Resources Technology Conference, San Antonio, Texas, August 1−3, 2016; Society of Exploration Geophysicists, American Association of Petroleum Geologists, Society of Petroleum Engineers, 2016; pp 1123−31, DOI: 10.15530/urtec-2016-2448210.

(21) Li, Z.; Liu, D.; Cai, Y.; Ranjith, P.G.; Yao, Y. Multi-scale quantitative characterization of 3-D pore-fracture networks in bituminous and anthracite coals using FIB-SEM tomography and X-ray μ-CT. *Fuel* **2017**, *209*, 43−53.

(22) Su, Y.; Zha, M.; Ding, X.; Qu, J.; Wang, X.; Yang, C.; et al. Pore type and pore size distribution of tight reservoirs in the Permian Lucaogou Formation of the Jimsar Sag, Junggar Basin, NW China. *Mar. Pet. Geol.* **2018**, *89*, 761−74.

(23) Bernard, S.; Horsfield, B.; Schulz, H. M.; Wirth, R.; Schreiber, A.; Sherwood, N. Geochemical evolution of organic-rich shales with increasing maturity: A STXM and TEM study of the Posidonia Shale (Lower Toarcian, northern Germany). *Mar. Pet. Geol.* **2012**, *31*, 70−89.

(24) Giesche, H. Mercury porosimetry: A general (practical) overview. *Particle and Particle Systems Characterization* **2006**, *23*, 9−19.

(25) Gunter, W. D.; Wiwehar, B.; Perkins, E. H. Aquifer disposal of CO_2-rich greenhouse gases: Extension of the time scale of experiment for CO_2-sequestering reactions by geochemical modelling. *Mineral. Petrol.* **1997**, *59*, 121−40.

(26) Lyu, Q.; Ranjith, P. G.; Long, X.; Ji, B. Experimental investigation of mechanical properties of black shales after CO_2-water-rock interaction. *Materials* **2016**, *9*, 663.

(27) Favero, V.; Laloui, L. Impact of CO_2 injection on the hydro-mechanical behaviour of a clay-rich caprock. *Int. J. Greenhouse Gas Control* **2018**, *71*, 133−41.

(28) Lu, Y.; Ao, X.; Tang, J.; Jia, Y.; Zhang, X.; Chen, Y. Swelling of shale in supercritical carbon dioxide. *J. Nat. Gas Sci. Eng.* **2016**, *30*, 268−75.

(29) Okamoto, I.; Li, X.; Ohsumi, T. Effect of supercritical CO_2 as the organic solvent on cap rock sealing performance for underground storage. *Energy* **2005**, *30*, 2344−51.

(30) Pettijohn, F. *Sedimentary Rocks*, 3rd ed.; Harper & Row: New York, 1975.

(31) Qin, C.; Jiang, Y.; Luo, Y.; Xian, X.; Liu, H.; Li, Y. Effect of Supercritical Carbon Dioxide Treatment Time, Pressure, and Temperature on Shale Water Wettability. *Energy Fuels* **2017**, *31*, 493−503.

(32) Carroll, S. A.; McNab, W. W.; Dai, Z.; Torres, S. C. Reactivity of Mount Simon Sandstone and the Eau Claire Shale Under CO_2 Storage Conditions. *Environ. Sci. Technol.* **2013**, *47*, 252−61.

(33) Yin, H.; Zhou, J.; Jiang, Y.; Xian, X.; Liu, Q. Physical and structural changes in shale associated with supercritical CO_2 exposure. *Fuel* **2016**, *184*, 289−303.

(34) Zhou, J.; Yang, K.; Tian, S.; Zhou, L.; Xian, X.; Jiang, Y.; et al. CO_2-water-shale interaction induced shale microstructural alteration. *Fuel* **2020**, *263*, 116642.

(35) Credoz, A.; Bildstein, O.; Jullien, M.; Raynal, J.; Pétronin, J. C.; Lillo, M.; et al. Experimental and modeling study of geochemical reactivity between clayey caprocks and CO_2 in geological storage conditions. *Energy Procedia* **2009**, *1*, 3445−52.

(36) Jiang, Y.; Luo, Y.; Lu, Y.; Qin, C.; Liu, H. Effects of supercritical CO_2 treatment time, pressure, and temperature on microstructure of shale. *Energy* **2016**, *97*, 173−81.

(37) Chareonsuppanimit, P.; Mohammad, S. A.; Robinson, R. L.; Gasem, K. A. M. High-pressure adsorption of gases on shales: Measurements and modeling. *Int. J. Coal Geol.* **2012**, *95*, 34−46.

(38) Kang, S. M.; Fathi, E.; Ambrose, R. J.; Akkutlu, I. Y.; Sigal, R. F. Carbon dioxide storage capacity of organic-rich shales. *SPE J.* **2011**, *16*, 842−55.

(39) Wang, T.; Tian, S.; Li, G.; Sheng, M.; Ren, W.; Liu, Q.; et al. Molecular Simulation of CO 2 /CH 4 Competitive Adsorption on Shale Kerogen for CO 2 Sequestration and Enhanced Gas Recovery. *J. Phys. Chem. C* **2018**, *122*, 17009−18.

(40) Mandelbrot, B. B. *The Fractal Geometry of nature*; WH Freeman: New York, 1983; Vol. *173*.

(41) Yang, R.; He, S.; Yi, J.; Hu, Q. Nano-scale pore structure and fractal dimension of organic-rich Wufeng-Longmaxi shale from Jiaoshiba area, Sichuan Basin: Investigations using FE-SEM, gas adsorption and helium pycnometry. *Mar. Pet. Geol.* **2016**, *70*, 27−45.

(42) Wang, X.; Jiang, Z.; Jiang, S.; Chang, J.; Zhu, L.; Li, X.; et al. Full-scale pore structure and fractal dimension of the Longmaxi shale from the southern Sichuan basin: Investigations using FE-SEM, gas adsorption and mercury intrusion porosimetry. *Minerals* **2019**, *9*, 1−27.

(43) Pfeifer, P.; Wu, Y. J.; Cole, M. W.; Krim, J. Multilayer adsorption on a fractally rough surface. *Phys. Rev. Lett.* **1989**, *62*, 1997−2000, DOI: 10.1103/PhysRevLett.62.1997.

(44) Qi, H.; Ma, J.; Wong, P. Z. Adsorption isotherms of fractal surfaces. *Colloids Surf., A* **2002**, *206*, 401.
(45) Kang, S. M.; Fathi, E.; Ambrose, R. J.; Akkutlu, I. Y.; Sigal, R. F. Carbon dioxide storage capacity of organic-rich shales. *SPE J.* **2011**, *16*, 842−55.
(46) Tien, C. *Thermodynamics of Adsorption*; Tien, C., Ed.; Butterworth-Heinemann: Boston, 1994; pp 9−14; DOI: 10.1016/B978-0-7506-9121-5.50007-0.
(47) Lee, H.; Shakib, F. A.; Shokouhimehr, M.; Bubach, B.; Kong, L.; Ostadhassan, M. Optimal Separation of CO_2/CH4/Brine with Amorphous Kerogen: A Thermodynamics and Kinetics Study. *J. Phys. Chem. C* **2019**, *123*, 20877−83.
(48) LeFever, J. A., LeFever, R. D., Nordeng, S. H. Chapter 1: Revised nomenclature for the Bakken Formation (Mississippian-Devonian), North Dakota. *The Bakken-Three Forks Petroleum System in the Williston Basin*; Rocky Mountain Association of Geologists, Denver, CO, 2011; pp 11−26.
(49) Pollastro, R. M.; Cook, T. A.; Roberts, L. N. R.; Lewan, M. D.; Anna, L. O.; et al. *Assessment of Undiscovered Oil Resources in the Devonian-Mississippian Bakken Formation, Williston Basin Province, Montana and North Dakota, 2008*; U.S. Geological Survey, 2008.
(50) Nordquist, J. W. *Mississippian Stratigraphy of Northern Montana*; 4th Annual Field Conference Guidebook, Billings Geological Society, 1953; pp 68−82.
(51) Halabura, S.; Buatois, L.; Angulo, S.; Piche, L. From Source to Trap: A Review of the Bakken Petroleum System, Upper Devonian-Mississippian, Southeastern Saskatchewan. *Saskatchewan Geological Survey - Summary of Investigations, 2007*; Saskatchewan Geological Survey, 2007; vol. *1*, pp 1−8.
(52) Nordeng, S. H.; Helms, L. D. *Bakken Source System−Three Forks Formation Assessment*; North Dakota Department of Mineral Resources; vol. *22*, p 2010.
(53) Lee, K. S.; Kim, T. H. *Integrative Understanding of Shale Gas Reservoirs; Integrative Understanding of Shale Gas Reservoirs; Springer International Publishing: Cham* **2016**, 21−41.
(54) Behar, F.; Beaumont, V.; De, B.; Penteado, H. L. Rock-Eval 6 Technology: Performances and Developments. *Oil Gas Sci. Technol.* **2001**, *56*, 111−134.
(55) Amankwah, K. A. G.; Schwarz, J. A. A modified approach for estimating pseudo-vapor pressures in the application of the Dubinin-Astakhov equation. *Carbon* **1995**, *33*, 1313−9.
(56) Fan, L.; Ziegler, T. Nonlocal Density Functional Theory as a Practical Tool in Calculations on Transition States and Activation Energies. Applications to Elementary Reaction Steps in Organic Chemistry. *J. Am. Chem. Soc.* **1992**, *114*, 10890−7.
(57) Do, D. D.; Do, H. D. Pore characterization of carbonaceous materials by DFT and GCMC simulations: A review. *Adsorpt. Sci. Technol.* **2003**, *21*, 389−424.
(58) Monson, P. A. Understanding adsorption/desorption hysteresis for fluids in mesoporous materials using simple molecular models and classical density functional theory. *Microporous Mesoporous Mater.* **2012**, *160*, 47−66.
(59) Ferreiro, J. P.; Wilson, M.; Vázquez, E. V. Multifractal Description of Nitrogen Adsorption Isotherms. *Vadose Zone J.* **2009**, *8*, 209−19.
(60) Liu, K.; Ostadhassan, M.; Zou, J.; Gentzis, T.; Rezaee, R.; Bubach, B.; et al. Multifractal analysis of gas adsorption isotherms for pore structure characterization of the Bakken Shale. *Fuel* **2018**, *219*, 296−311.
(61) Sahouli, B.; Blacher, S.; Brouers, F. Fractal surface analysis by using nitrogen adsorption data: The case of the capillary condensation regime. *Langmuir* **1996**, *12*, 2872−4.
(62) Mahamud, M. M.; Novo, M. F. The use of fractal analysis in the textural characterization of coals. *Fuel* **2008**, *87*, 222−31.
(63) Jaroniec, M. Evaluation of the Fractal Dimension from a Single Adsorption Isotherm. *Langmuir* **1995**, *11*, 2316−7.
(64) Sakhaee-Pour, A.; Li, W. Fractal dimensions of shale. *J. Nat. Gas Sci. Eng.* **2016**, *30*, 578−82.
(65) Grigg, R. B.; Svec, R. K. CO_2 Transport Mechanisms in CO_2/Brine Coreflooding. *SPE Annual Technical Conference and Exhibition 2006*; Society of Petroleum Engineers, 2006; vol. *10*; DOI: 10.2118/103228-MS.
(66) Morse, J. W.; Mackenzie, F. T. Geochemistry of sedimentary carbonates. *Geochemistry of Sedimentary Carbonates* **1990**, 96822.
(67) Gharbi, O.; Bijeljic, B.; Boek, E.; Blunt, M. J. Changes in pore structure and connectivity induced by CO_2 injection in carbonates: A combined pore-scale approach. *Energy Procedia* **2013**, *37*, 5367−78.
(68) Gregg, S. J.; Sing, K. S. W.; Sing, K. S. *Adsorption, Surface Area and Porosity*; Academic Press: London, 1982; Vol. *86*; DOI: 10.1002/bbpc.19820861019.
(69) Landers, J.; Gor, G. Y.; Neimark, A. V. Density functional theory methods for characterization of porous materials. *Colloids Surf., A* **2013**, *437*, 3−32.
(70) Cychosz, K. A.; Guillet-Nicolas, R.; García-Martínez, J.; Thommes, M. Recent advances in the textural characterization of hierarchically structured nanoporous materials. *Chem. Soc. Rev.* **2017**, *46*, 389−414.
(71) Sing, K. S. W.; Everett, D. H.; Haul, R. A. W.; Moscou, L.; Pierotti, R. A.; Rouquerol, J.; et al. Reporting Physisorption Data for Gas/Solid Systems with Special Reference to the Determination of Surface Area and Porosity. *Pure Appl. Chem.* **1985**, *57*, 603−19.
(72) Chalmers, G. R.; Bustin, R. M.; Power, I. M. Characterization of gas shale pore systems by porosimetry, pycnometry,surfacearea,and-field emission scanning electron microscopy/ transmission electron microscopy image analyses: Examples from the Barnett, Woodford, Haynesville, Marcellus,andDoig units. *AAPG Bull.* **2012**, *96*, 1099−119.
(73) Liu, K.; Ostadhassan, M.; Cai, J. Characterizing Pore Size Distributions of Shale. In *Petrophysical Characterization and Fluids Transport in Unconventional Reservoirs*; Elsevier, 2019; pp 3−20.
(74) Li, Z.; Shen, X.; Qi, Z.; Hu, R. Study on the pore structure and fractal characteristics of marine and continental shale based on mercury porosimetry, N2 adsorption and NMR methods. *J. Nat. Gas Sci. Eng.* **2018**, *53*, 12−21.
(75) Major, J. R.; Eichhubl, P.; Dewers, T. A.; Olson, J. E. Effect of CO_2−brine−rock interaction on fracture mechanical properties of CO_2 reservoirs and seals. *Earth Planet. Sci. Lett.* **2018**, *499*, 37−47.
(76) Zou, Y.; Li, S.; Ma, X.; Zhang, S.; Li, N.; Chen, M. Effects of CO_2−brine−rock interaction on porosity/permeability and mechanical properties during supercritical-CO_2 fracturing in shale reservoirs. *J. Nat. Gas Sci. Eng.* **2018**, *49*, 157−68.
(77) Jean, J. S.; Wang, C. L.; Hsiang, H. I.; Li, Z.; Yang, H. J.; Jiang, W. T.; et al. Experimental investigation of trace element dissolution in formation water in the presence of supercritical CO_2 fluid for a potential geological storage site of CO_2 in Taiwan. *J. Nat. Gas Sci. Eng.* **2015**, *23*, 304−14.
(78) Lu, Y.; Ao, X.; Tang, J.; Jia, Y.; Zhang, X.; Chen, Y. Swelling of shale in supercritical carbon dioxide. *J. Nat. Gas Sci. Eng.* **2016**, *30*, 268−75.

https://dx.doi.org/10.1021/acs.energyfuels.0c03763
Energy Fuels XXXX, XXX, XXX−XXX